BoundaryNet: Extraction and Completion of Road Boundaries With Deep Learning Using Mobile Laser Scanning Point Clouds and Satellite Imagery

Article *in* IEEE Transactions on Intelligent Transportation Systems · February 2021

DOI: 10.1109/TITS.2021.3055366

CITATIONS
2

READS
344

6 authors, including:

Lingfei Ma
Central University of Finance and Economics
41 PUBLICATIONS **506** CITATIONS
SEE PROFILE

Ying Li
Beijing Institute of Technology
20 PUBLICATIONS **338** CITATIONS
SEE PROFILE

Jonathan Li
University of Waterloo
547 PUBLICATIONS **9,641** CITATIONS
SEE PROFILE

José Marcato Junior
Universidade Federal de Mato Grosso do Sul
128 PUBLICATIONS **754** CITATIONS
SEE PROFILE

BoundaryNet: Extraction and Completion of Road Boundaries With Deep Learning Using Mobile Laser Scanning Point Clouds and Satellite Imagery

Lingfei Ma, *Student Member, IEEE*, Ying Li, Jonathan Li, *Senior Member, IEEE*, José Marcato Junior, *Member, IEEE*, Wesley Nunes Gonçalves, *Member, IEEE*, and Michael A. Chapman, *Senior Member, IEEE*

***Abstract*— Robust road boundary extraction and completion play an important role in providing guidance to all road users and supporting high-definition (HD) maps. The significant challenges remain in remarkable and accurate road boundary recovery from poor road boundary conditions. This paper presents a novel deep learning framework, named BoundaryNet, to extract and complete road boundaries by using both mobile laser scanning (MLS) point clouds and high-resolution satellite imagery. First, road boundaries are extracted by conducting a curb-based extraction method. Such extracted 3D road boundary lines are used as inputs to feed into a U-shaped network for erroneous boundary denoising. Then, a convolutional neural network (CNN) model is proposed to complete the road boundaries. Next, to achieve more complete and accurate road boundaries, a conditional deep convolutional generative adversarial network (c-DCGAN) with the assistance of road centerlines extracted from satellite images is developed. Finally, according to the completed road boundaries, the inherent road geometries are calculated. The proposed methods were evaluated using satellite imagery and four MLS point cloud datasets with varying densities and road conditions in urban environments. The quality evaluation metrics of 82.88%, 82.43%, 88.86%, and 84.89% were achieved for four data sets. The experimental results indicate that the BoundaryNet model can provide a promising solution for road boundary completion and road geometry estimation.**

***Index Terms*— Mobile laser scanning, point clouds, road boundary, extraction, completion, road geometry, deep learning, satellite image.**

Manuscript received May 26, 2020; revised September 25, 2020 and December 8, 2020; accepted January 15, 2021. This work was supported in part by the National Natural Science Foundation of China under Grant 41871380. The Associate Editor for this article was H. G. Jung. *(Corresponding author: Jonathan Li.)*

Lingfei Ma is with the Engineering Research Center of State Financial Security, Ministry of Education, Central University of Finance and Economics, Beijing 102206, China, and also with the Department of Geography and Environmental Management, University of Waterloo, Waterloo, ON N2L 3G1, Canada (e-mail: l53ma@cufe.edu.cn).

Ying Li is with the Department of Geography and Environmental Management, University of Waterloo, Waterloo, ON N2L 3G1, Canada (e-mail: y2424li@uwaterloo.ca).

Jonathan Li is with the Engineering Research Center of State Financial Security, Ministry of Education, Central University of Finance and Economics, Beijing 102206, China, also with the Department of Geography and Environmental Management, University of Waterloo, Waterloo, ON N2L 3G1, Canada, and also with the Fujian Key Laboratory of Sensing and Computing for Smart Cities, School of Informatics, Xiamen University, Xiamen FJ 361005, China (e-mail: junli@xmu.edu.cn).

José Marcato Junior and Wesley Nunes Gonçalves are with the Faculty of Engineering, Architecture and Urbanism and Geography, Federal University of Mato Grosso do Sul, Campo Grande 79070-900, Brazil (e-mail: jose.marcato@ufms.br; wesley.goncalves@ufms.br).

Michael A. Chapman is with the Department of Civil Engineering, Ryerson University, Toronto, ON M5B 2K3, Canada (e-mail: mchapman@ryerson.ca).

Digital Object Identifier 10.1109/TITS.2021.3055366

I. Introduction

URBAN roads, as one of the essential public infrastructures, motivate rapid urban sprawl and create notable economic and social benefits [1]. Moreover, detailed road inventories are commonly applied to support extensive applications, such as city planning, construction surveying, smart cities, and advanced driver-assistance systems (ADAS) [2]. Mobile laser scanning (MLS) systems that comprise Light Detection and Ranging (LiDAR) sensors can capture high-density 3D point clouds with mm-level accuracy in large-scale urban environments [3]. Such point clouds have been widely used for many transportation-related studies, including pavement inspection [4], road marking classification [5], road object detection and segmentation [6], road geometry modeling [7], and road boundary extraction [8]. As a crucial component of road networks, road boundaries demarcate allowable driving zones and provide auxiliary road information to promote high-definition (HD) maps and fully autonomous vehicles (AVs). Accordingly, road boundary extraction is generally implemented through extracting road surfaces, followed by road curb detection from MLS point clouds. Although remarkable improvement has been achieved, most of the off-the-shelf methods cannot accurately and completely extract road boundaries, due to occlusions and point density variations during raw MLS data acquisition [9]. Thus, in this paper, we mainly focus on the theoretical and methodological problems of road boundary extraction and completion using MLS point clouds and satellite imagery.

Many studies have been conducted to estimate and recover incomplete road boundaries [10]–[12]. One of the most straightforward ways is to collect multiple MLS point

Fig. 1. Illustrations of road boundaries with gaps obtained from MLS point clouds. The first row represents digital images, and the second row indicates the extracted boundaries (blue lines) from MLS point clouds. Yellow boxes show the missing parts in the extracted road boundaries. (a) Incomplete boundaries due to occlusions. (b) Worn road curbs. (c) A connection area between bikeways and roadways.

clouds. However, it is considerably cost-intensive and labor-consuming. Moreover, some interpolation methods, such as linear interpolation, polynomial interpolation, and B-spline curves, cannot deliver the robust solutions for road boundary recovery, especially in complicated crossroads and curved road sections [12]. Many researchers concentrated on extracting road surfaces or road centerlines from aerial and orbital remotely sensed imagery. In urban environments, roads extracted from satellite and aerial images are usually inaccurate and incomplete because of imperfect lighting conditions, various terrain factors, and partial occlusions caused by roadside trees [13]. Furthermore, different image resolutions have significant impacts on road boundary extraction. Specifically, images captured with low resolutions could result in fuzzy ground object features, while high-resolution images also bring in dilemmas and uncertainties regarding various influential factors (e.g., high computational cost).

Compared to camera-based mobile mapping systems, MLS systems are effective to collect 3D point clouds in varying road conditions. The point density obtained from high-end MLS systems can reach up to 10,000 pts/m^2 at a wide moving speed range of 40-100 km/h, while it poses enormous difficulties for both airborne and terrestrial laser scanning (ALS/TLS) systems to provide such high surveying adaptability and measuring precision [14]. Roads extracted from ALS point clouds are usually broken lines because of the distortions, point density and intensity variations, and noisy outliers [15], [16]. Moreover, sparse and unevenly distributed TLS point clouds make effective and robust road extraction quite challenging. Global Positioning System (GPS) data, which provides spatial trajectory and the full coverage of roads, have been typically employed to extract road boundaries and centerlines. Hashemi [17] developed an automatic algorithm to fix the topological errors to construct accurate road and pedestrian networks using the geometrical traits obtained from the crowd-sourced GPS data. Nevertheless, both accuracy and completeness of extracted road boundaries using spatial trajectory data and crowd-sourced GPS data (e.g., taxi GPS data) are still unsatisfied because of the inevitable system positioning error and multipath effects in urban road scenarios.

Urban roads, segmented from various data sources, indicate various strengths and limitations. As illustrated in Fig. 1, there are three key challenges to efficiently and robustly extract and complete road boundaries from MLS point clouds: (1) Road boundary data is incomplete due to occlusions caused by road participants (e.g., pedestrians and cyclists) and roadside infrastructures, or the limited scanning ranges from onboard sensors. (2) Some urban roads with low curbs or worn curbs also lead to incomplete road boundaries using different threshold-based extraction methods (e.g., supervoxel-based method [11] and curb-based method [12]). Because it is difficult to determine multi-scale and suitable thresholds to deal with various road curbs. (3) Moreover, due to the varieties and uncertainties of missing parts in urban road boundaries (e.g., large gaps caused by road damages, connection areas, and irregular road structures), it poses significant difficulties to ascertain if these gaps should be completed or not. To overcome these challenges, we explore the practicality of road boundary extraction and completion using MLS point clouds and satellite images. Satellite images can assist MLS point clouds to generate more complete and correct road boundaries. This paper defines that regular and large gaps should be recovered, while connection areas are not. However, these satellite images and MLS clouds captured by different sensors at different times and in varying ambient illumination conditions, cause the effective data fusion challenging [18].

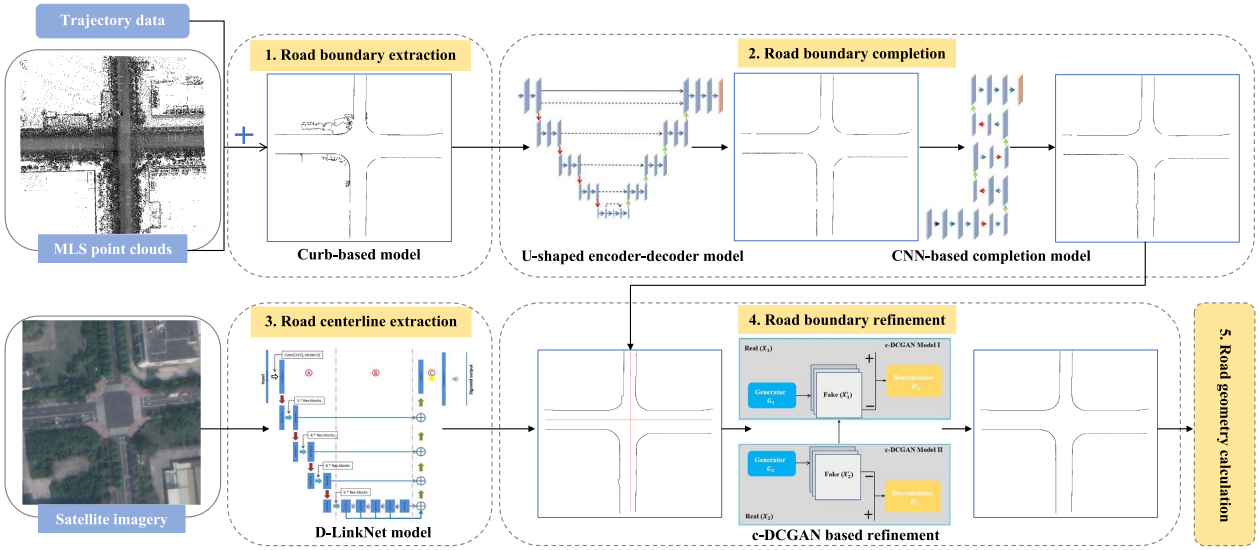

Fig. 2. The workflow of the proposed BoundaryNet model that contains four sections: road boundary extraction using a curb-based method; road boundary completion by conducting a U-shaped encoder-decoder network and a CNN-based network; road centerline extraction from satellite images by using a D-LinkNet model; and road boundary refinement by performing a c-DCGAN model. Finally, road geometries are calculated.

Previous road boundary extraction studies showed the potential of data fusion from multiple sensors [19], [20]. These methods have significantly improved the road boundary extraction accuracy by introducing spectral or texture information, but they still cannot deal with existing gaps in road boundaries. For road boundary completion, the existing methods have certain limitations [8]. Considerable challenges still exist to provide promising solutions for road boundary completion, especially in complex curved road scenes. Therefore, it is increasingly necessary to introduce an effective and robust method for road boundary completion.

We propose a novel deep learning (DL)-based framework, named BoundaryNet, comprising the following four modules: (1) curb-based road boundary extraction, (2) CNN-based road boundary completion, (3) the D-LinkNet based road centerline extraction, and (4) the conditional deep convolutional generative adversarial network (c-DCGAN) based road boundary refinement. Fig. 2 shows the detailed workflow of BoundaryNet. More specifically, 3D road boundaries are segmented from point clouds as the inputs of the whole framework. The extracted road boundaries that always contain many erroneous lines, are firstly removed using a revised U-shaped encoder-decoder neural network, according to the images projected from 3D point clouds of road boundaries. Next, a CNN-based downsampling and upsampling model enabling to capture more distinctive features of line segments (e.g., curvature and connectivity), is developed to identify and restore the missing parts. Then, because of the imperfect local details of road boundaries resulting from the CNN-based completion model, such road boundaries are further refined using a c-DCGAN model, with the assistance of the road centerlines obtained from high-resolution satellite images. Finally, according to the completed road boundaries, inherent road geometries including both horizontal and vertical road alignments, are estimated to support road maintenance and traffic safety. Unlike 3D point-based methods suffering from incomplete data collection and point density and intensity variations, a deep learning-based framework combining both MLS point clouds and satellite images is developed, which can more robustly extract and complete road boundaries, and accurately estimates the road characteristics in large-scale urban environments.

II. Related Work

A. Road Boundary Extraction

Generally, the commonly applied boundary extraction methods are categorized into three groups: remotely sensed image-driven methods [21], [22], 3D point-driven methods [23]–[26], and multi-source data-driven methods [27], [28]. Remotely sensed imagery acquired by various platforms and sensors, such as vehicle-based imagery, drone-based imagery, satellite imagery, and airborne or satellite synthetic aperture radar (SAR) imagery, provide significant spectral, spatial, and texture information for the robust and effective road feature extraction in large-scale terrains. For instance, in [13], a Multi-supervised Generative Adversarial Network (MsGAN) framework was proposed to extract road boundaries and centerline maps from satellite images, which is trained by considering the topology and spectral information of roads. By estimating an approximate prediction of the road edges for guidance, an anisotropic shock filtering framework was developed to extract roads [29]. Additionally, a graph-driven neural turtle graphics network was introduced in [30] to detect urban road layouts on the SpaceNet dataset, while nodes in the graph indicate spatial control points of the road networks and edges represent road segments. However, various environmental and topological factors, including ambient lighting conditions, the complexity of road scenarios, and undulating terrains, have remarkable impacts on the road boundary extraction performance from 2D images.

Meanwhile, 3D point clouds acquired by MLS, ALS, and TLS systems have been an appropriate data source for road boundary extraction. In [11], a two-stage method was developed for 3D road boundary extraction from MLS point clouds in complex road scenes. First, supervoxels were generated based on smooth seed points and different geometric and spatial attributes. Road boundaries were then extracted by performing the α-shape algorithm, followed by the graph-cut related energy minimization algorithm. In addition, a multi-thresholding based method was proposed in [31] to extract lane markings based on road construction standards. The spatial density filtering and geometric filtering algorithms were then conducted for noisy point removal.

Moreover, according to independent patches of the road network, 3D road maps were generated in [32] by using cardinal splines under continuity constraints and an attractor function for curb detection from both ALS and MLS point clouds. However, it is difficult to accurately and completely extract road boundaries regarding unordered and noisy point clouds. The information loss is inevitable during the process of voxelization and occlusions.

Furthermore, because of the limitations of employing a single data source, some methods that consider multi-source data are essential to obtain rich road information and complete road boundaries with high accuracy and robustness. In [33], by constructing mapping layers between LiDAR's imagery views and camera's views, a two-view fusion-based CNN was proposed to robustly extract road networks and estimate road areas in urban scenes. In [34], a conditional random forest (CRF)-based method was proposed to extract color and range features for road network extraction using both LiDAR point clouds and camera images. Meanwhile, based on a hierarchical residual fusion strategy, a fully convolutional network (FCN)-based framework was introduced in [35] to extract inherent features and merge the feature maps learned from the LiDAR-camera data for accurate road detection. In [19], a transfer learning-based neural network was used for road feature encoding and a U-Net framework for road centerline and edge extraction by integrating aerial images with taxi trajectories.

Additionally, an intensity-based multi-threshold method [20] was proposed to extract lane markings (e.g., road boundaries), and then fused the extracted lane markings from MLS point clouds with RGB-camera images for accurate lane width estimation and road boundary measurement. Moreover, a novel tightly-coupled perception-planning framework was developed in [36] to detect road lane boundaries based on the LiDAR-camera-GPS data fusion to support autonomous vehicle navigation. Although such methods have significantly improved road boundary extraction accuracy by introducing spectral or texture information, they still cannot deal with existing road boundary gaps.

B. Road Boundary Completion

To fill these existing gaps caused by occlusions and method drawbacks and enhance road boundary completeness, an energy function was employed in [37] for the candidate curb point segmentation from MLS point clouds and further refined these candidate points using a least-cost path model. Likewise, in [12], a B-spline least-squares fitting method was performed to generate smooth road boundaries from candidate road curb points. However, it is challenging for such methods to deal with complex road sections (e.g., compound or spiral road curves). Inspired by image inpainting, in [8], a convolutional neural network (CNN)-based model was first proposed to complete gaps and recover road boundaries from 3D point clouds. Then, a conditional generative adversarial network (cGAN) framework was implemented to deal with the uncertainties of missing parts of road boundaries and refine them accordingly. The existing methods have certain limitations and considerable challenges to provide promising solutions for road boundary completion, especially in complex curved road scenes. Therefore, it is increasingly necessary to introduce an effective and robust method for road boundary completion.

III. Methods

A. Curb-Based and U-Shaped Boundary Recovery

According to our previous work [12], a revised curb-based road boundary extraction approach was proposed using a data slicing structure from 3D point clouds. Firstly, depending on the MLS trajectory, the raw mobile LiDAR data were horizontally divided as a series of point cloud blocks, in which corresponding data profiles were created at predefined widths. Then, the point clouds in these data profiles were projected onto the XY plane. Such data profiles were gridded to generated pseudo scan lines, and principal points were accordingly ascertained in grid cells. Next, road curb points were segmented from pseudo scan lines by analyzing both slope and elevation differences. Finally, a B-spline interpolation algorithm was used to fit the extracted road curb points into continuous boundary lines. Therefore, in this paper, this curb-based method is adopted for road boundary extraction.

For complex urban road environments, the extracted road boundaries have multiple objects (e.g., road markings, cracks, and roadside objects) and erroneous lines with occlusions from road users, which brings in considerable difficulties in road boundary extraction. Due to varying road design standards across different regions and the morphological irregularity of erroneous lines, it is quite challenging to completely and effectively extract road boundaries from massive and unordered 3D point clouds by using the existing rule-based methods [38]–[40].

Based on the symmetric encoder-decoder framework and skip connection operations, the U-Net model [41] has been demonstrated that it enables to deliver promising solutions for image segmentation tasks. Compared to patch-based image segmentation methods (e.g., V-Net [42]), the proposed U-shaped neural network can use both location and context simultaneously in a global scale, and it performs well with relatively few training samples. Moreover, this proposed U-shaped network consumes low computational cost and thus causes increasing processing speeds.

Herein, a revised U-shaped encoder-decoder deep learning framework is introduced that learns inherent features to

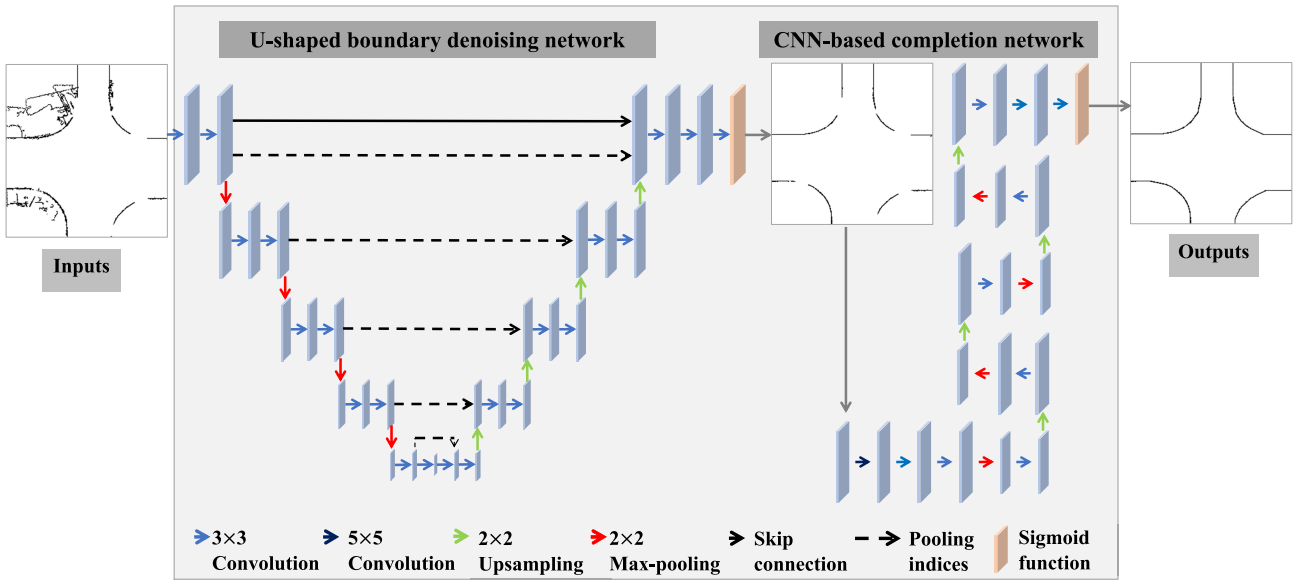

Fig. 3. Structures of the U-shaped network and the CNN-based completion network.

separate road boundaries from the erroneous lines (see Fig. 3). To this end, the extracted 3D road boundaries are first transformed into a 2D image in a horizontal XY plane with a pixel size $S_{\epsilon 1}$. Thus, the complicated erroneous line removal problem is perceived as a straightforward binary image classification task. That is, road boundaries are regarded as foreground and other lines as background. The proposed U-shaped neural network contains encoder and decoder sections. Each encoder layer performs 2D convolutions with a kernel size of 3 $\times$ 3 for spatial feature encodings, while each decoder layer conducts 2D deconvolution (2 $\times$ 2 kernel size) and convolution (3 $\times$ 3 kernel size) operations for segmentation feature map construction. As shown in Fig.3, instead of only using skip connection in the U-Net model, we also employ pooling indices connection to feed max-pooling indices (2 $\times$ 2 filter size) derived from the corresponding encoders into decoders for non-linear upsampling operations. Such max-pooling indices can significantly decrease the number of parameters facilitating end-to-end training. The dropout operation is implemented to reduce the over-fitting problem. The binary cross-entropy (BCE) function is employed to guide the model refinement calculated by:

$$\mathrm{L}(\mathrm{y}, \hat{y}) = \frac{1}{N}\sum_{\mathrm{i}=1}^{N}\left(y \times \log \hat{y}_i + (1-y) \times \log\left(1-\hat{y}_i\right)\right) \quad (1)$$

where N indicates the total number of pixels in input images, y is the real value, and $\hat{y}_i$ represents the predicted value. The rasterized 2D images, as training data, are augmented through scaling, rotation, and crop operations, and then resized to 512 $\times$ 512 pixels before feeding into the denoising network. The training samples are generated by selecting the segmented road boundary pixels as inputs, which are manually labeled in 2D images. In the training stage, the dropout rate, batch size, initial learning rate, and epoch are 0.5, 4, 0.0001, and 300, respectively.

B. CNN-Based Road Boundary Completion

Therefore, road boundaries are successfully extracted from MLS point clouds using the curb-based road boundary extraction method, followed by the U-shaped denoising neural network. Still, the gaps in extracted road boundaries with varying structures (e.g., lengths and curvatures) cause considerable dilemmas in direct and robust road boundary completion. To date, many researchers are dedicating themselves to image recovery and inpainting based on deep learning-based methods [43]–[45], which have achieved good performance. In [46], an end-to-end network was presented to detect gaps in deteriorated line drawings and recover them accordingly. This method indicated superior performance in line drawing restoration and curvature and thickness conservation. Inspired by line inpainting, a novel CNN-based model is proposed to complete road boundaries in 2D space. Unlike other deep learning-based methods (e.g., FCNs and auto-encoders [47]) are designed to restore natural images with rich texture and gradient information, the proposed CNN-based model can perform remarkably better for image restoration if images are sparse. Moreover, due to the varieties and uncertainties of missing parts in urban road boundaries, the proposed model can effectively fill most gaps with various sizes and structures.

Fig. 3 shows that a CNN-based downsampling and upsampling model is developed to identify and fill the missing parts based on the road boundary extraction results obtained after the erroneous line removal. This model contains convolution, max pooling, and upsampling layers. More specifically, all the convolution layers employ a 3 $\times$ 3 kernel size, aside from the first layer, conducting a 5 $\times$ 5 kernel size. Moreover, all convolution layers utilize the Rectified Linear Unit (ReLU) as activation functions, aside from the last one, where the Sigmoid function is employed instead. In the training stage, batch normalization is conducted after each convolution operation, except for the final one. The 2 $\times$ 2 max pooling

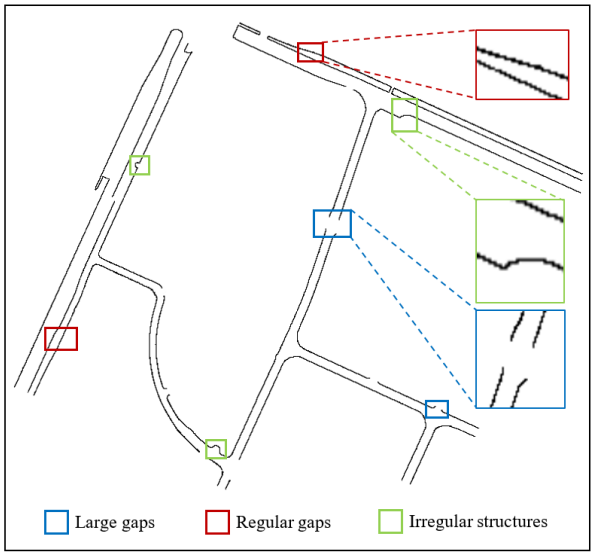

Fig. 4. Road boundary completion results using CNN-based network.

layers, downsampling by 1/2 size of the feature maps, are utilized for feature encoding and structure recognition of road boundaries from a larger region. Instead of deconvolution layers, we use the nearest neighbor upsampling method to enlarge the image resolution of outputs. Notably, we do not employ fully connected (FC) layers, the image sizes of inputs and outputs are not fixed, resulting in output images of the same size as the inputs. The model is trained by employing the mean squared error (MSE) as the cost function, which calculates the difference between input S and output S'_p as follows:

$$\text{loss}(S, \hat{S}) = \frac{1}{M} \sum_{p \in M} \left(S_p - S'_p \right)^2 \tag{2}$$

where M is the total number of pixels in the input image, and S_p and S'_p represent the values at pixel p in the input and the output images, respectively. Because of the limited number of training data, we use the same training dataset used in [46]. Finally, to obtain smooth and continuous boundary lines, only the completed 2D pixels by the CNN-based model are utilized to convert and add back to 3D road boundary point clouds.

C. Road Boundary Refinement

Because of the complexities and uncertainties in urban roads, the CNN-based completion method cannot fully complete the missing parts in images, particularly for large gaps. As shown in Fig. 4, the dilemmas are concluded in the following aspects: (1) some large missing parts should be completed (see blue boxes), (2) regular gaps should not be completed (see red boxes), and (3) irregular road structures (see green boxes). Therefore, the road boundaries that are completed by using the above completion method should be further refined.

Rapid data collection, large area coverage, and detailed feature characteristics with rich geospatial and texture information on the ground are strengths of remotely sensed imagery. Therefore, the high-resolution satellite images are employed to determine gaps, whether they should be further completed or not. Herein, satellite images are used to extract road centerlines, representing urban road structures in some ways, for the road boundary refinement in case of complexities and uncertainties. Furthermore, the module Georeferencing in ArcGIS Desktop v10.5.1 is performed to fuse satellite images and point clouds. The geospatial information of satellite images is calibrated with the assistance of the rasterized point clouds.

1) Road Centerline Extraction: The high-resolution satellite images are utilized to extract road centerlines that indicate a geometric topology of the road. Such centerlines are therefore used to handle the uncertainties of missing parts and guide the boundary refinement. To this end, the D-LinkNet method proposed in [48] is employed to segment roads from satellite imagery. This network comprises three modules, namely encoder, dilation part, and decoder. Specifically, the encoder module contains five downsampling layers that use ResNet34 [49] pre-trained on the ImageNet dataset to learn shallow features and generate feature maps. The 2×2 max pooling layers are used to downsample the inputs from the size of 1024×1024 to 32×32. Then, as shown in Fig. 5, the dilation module comprises dilated convolution in both parallel mode and cascade mode to increase the receptive field and preserve the detailed spatial information. All the dilated convolution layers employ a 3×3 kernel size, with a dilation rate of 1, 2, 4, and 8 in the center. The decoder module is the same as the original D-LinkNet, which is cost-effective and computation-efficient. The transposed convolution layers are used to restore the feature maps to the resolution of 1024×1024. Each convolution layer uses ReLU as activation functions, except for the last layer, which uses the Sigmoid function. Adam is used as the optimizer. Moreover, this model applies BCE and dice coefficient as the loss function. BCE is calculated by using Eq.1, and the dice coefficient loss is computed as follows:

$$\text{Dice} = \frac{2 \sum_i^N p_i g_i}{\sum_i^N p_i + \sum_i^N g_i} \tag{3}$$

where N is the total number of pixels in the input image, and p_i and g_i indicate the values at pixel i in the predicted binary segmentation images and ground truth images, respectively.

The DeepGlobe Road Extraction dataset [50] is used to increase the number of training data. The testing images were acquired from Google Earth with a pixel size of 50 cm. During the training phase, the initial learning rate, batch size, and epoch are 0.0001, 2, and 150, respectively.

A morphological thinning algorithm introduced in [51] is conducted to generate road centerlines, based on the extracted road segments from satellite images. Given each road pixel p_1 and its eight-connected neighbors, i.e., p_2 to p_9 (see Fig. 6(a)), the main procedure of this thinning algorithm is to traverse each pixel of the road segment images. In each pass, the road pixel p_i is removed if it meets the following criteria:

i. $2 \leq N(p_1) \leq 6$;
ii. $\delta(p_1) = 1$;
iii. $p_2 \times p_4 \times p_8 = 0$ or $\delta(p_2) \neq 1$;
iv. $p_2 \times p_6 \times p_8 = 0$ or $\delta(p_8) \neq 1$.

where $N(p_1)$ indicates the crossing number of road pixels among pixels p_2 to p_9, and $\delta(p_i)$ represents the discriminant

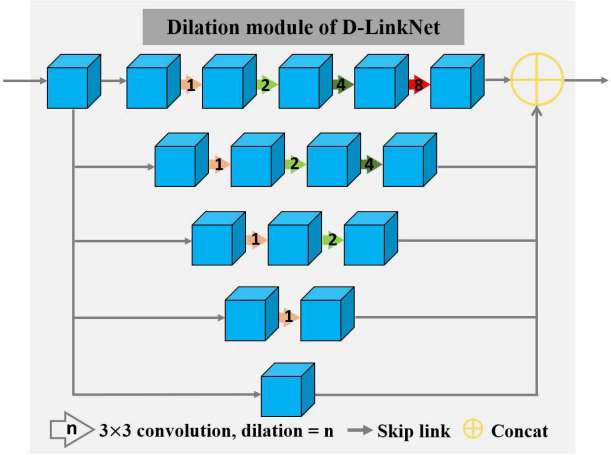

Fig. 5. The dilation module of D-LinkNet. It comprises dilated convolution in both parallel mode and cascade mode, and the receptive fields are different in different layers, enabling this model to combine features at various levels. From bottom to top, the receptive field is 1, 3, 7, 15, and 31, respectively.

condition, $i = 1$, 2, and 8, respectively. As shown in Fig. 6(b), the following condition is examined: the upper-left neighbor and the upper neighbor of the pixel p_i is a road pixel (with a pixel value of 1) and an empty pixel (with a pixel value of 0), respectively. Meanwhile, Figs. 6(c)-(i) illustrate different eight-connected discriminant conditions. Accordingly, $\delta(p_i) = 1$, if only one condition is satisfied. Otherwise, $\delta(p_i) = 0$. Thus, based on the eight-connected schema, road centerlines are generated from the extracted road segments.

The strengths of this thinning algorithm are both straightforward and fast to conduct. However, the extracted road centerlines usually generate some spurs that decrease the correctness and smoothness of roads. Thus, the least-square curve fitting algorithm is performed to obtain smooth and accurate road centerlines for irregular road networks. The least-square fitting algorithm takes the following form for each road segment:

$$\min \sum_{i=1}^{N} y_i - \left(p_1 x_i^n + p_2 x_i^{n-1} + \cdots + p_n x_i + p_{n+1}\right) \quad (4)$$

where N denotes the total number of pixels in road segments, x_i and y_i are the row number and the column number of the pixel i. After solving Eq. 4, the estimation is determined by:

$$\widehat{y}_i = \text{round}\left(p_1 x_i^n + p_2 x_i^{n-1} + \cdots + p_n x_i + p_{n+1}\right) \quad (5)$$

where $\widehat{y}_l$ denotes the column number of the pixel i after curve fitting.

Depending on the global coordinate system of satellite images, the generated road centerlines from these images are transformed to 3D point clouds by setting the height values to zero and then merged with road boundaries. Although high-rise objects and roadside trees inevitably occlude urban roads in satellite imagery, the generated road centerlines can still refine road network structures and provide significant road boundary refinement guidance.

2) c-DCGAN-Based Road Boundary Refinement: To tackle the complexities of missing parts and restore incomplete road boundaries, we further decide whether the restored gaps are refined with the assistance of the road centerlines. In this paper, the road boundaries are restored to the original structure if the road centerline across the gaps. Therefore, erroneous completions can be handled. Still, it is challenging to solve the dilemmas of incomplete gaps and irregular completion structures.

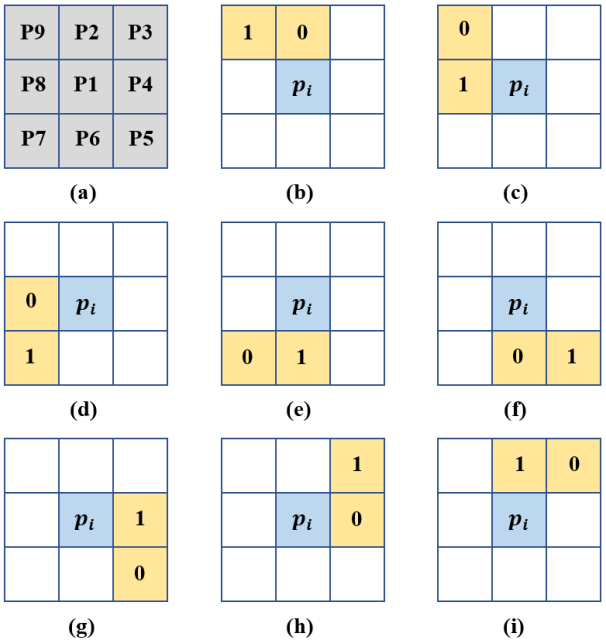

Fig. 6. Schema of the eight-connected morphological thinning algorithm. (a) A road pixel p_i and its eight neighbors. (b)-(i) indicate various discriminant conditions, respectively.

Generative adversarial network (GAN) models have indicated the extensive applications in image translation and image restoration domains [52]. The conditional deep convolutional GAN network is adopted, as an extended work of the DCGAN model, to deal with irregular completion structures (i.e., an image translation task) and incomplete gaps (i.e., an image restoration task). Through introducing conditions in DCGAN models, the c-DCGAN model can accelerate the training process that produces conditional outputs using the superior feature extraction ability of deep convolutional networks. The c-DCGAN model is capable of restoring the incomplete road boundaries with detailed information, particularly for curved road sections, which makes the rule-based refinement methods [12] challenging.

The DCGAN model consists of two adversarial modules, i.e., generator model G, and discriminator model D. Specifically, a generator G generates outputs, and a discriminator D distinguishes them as "real/fake" samples as much as possible. The adversarial competition between G and D is determined by:

$$\min_G \max_D L(D, G) = \mathbb{E}_{X \sim P_{\text{data}}(x)}[\log D(x)] + \mathbb{E}_{z \sim P_z(z)}[\log(1 - D(G(z)))] \quad (6)$$

where the discriminator endeavors to maximize the loss value, i.e., $D_G^* = \arg\max_D L(G, D)$, while the generator minimizes it, i.e., $G^* = \arg\min_G L\left(G, D_G^*\right)$. In the process of training

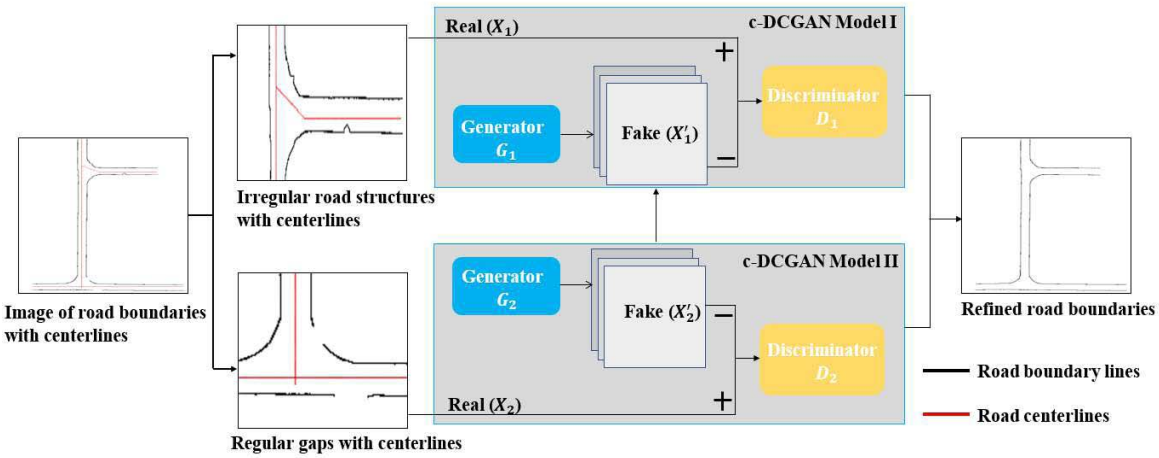

Fig. 7. Structure of the c-DCGAN road boundary refinement network.

D, G operates in a feed-forward pattern without backpropagation, and vice versa to process G.

Compared to the standard GAN model, the DCGAN model is more stable to train, resulting in generators that produce sensical outputs. Briefly, all convolutional net is performed by replacing deterministic spatial pooling operations (e.g., max pooling) with strided convolutions, enabling the model to encode both spatial downsampling and upsampling. Moreover, batch normalization is adopted to solve poor initialization and improve gradient flows in deep hidden layers. Instead of ReLU, D uses Leaky ReLU as activation functions. G uses ReLU, except for the output layer, where a $tanh$ function is used instead.

The c-DCGAN network extends the DCGAN model by generating feature maps from a random noise vector υ and a condition c to an output y. For c-DCGAN, road boundary refinement is performed by transforming images with incomplete road boundary lines and centerlines, into refined images with ground-truth road boundary lines. Herein, the condition c defines images with incomplete road boundary lines and centerlines. υ is a random noise vector. The result y indicates images with ground-truth road boundary lines. This c-DCGAN model can be easily applied to other road types by using a different condition c. Furthermore, only a small number of training samples are required to feed into the c-DCGAN model for road boundary refinement. Such training samples are: (1) cropped complete road boundaries and centerlines, (2) imperfect boundary lines (i.e., incomplete gaps and irregular completion structures) and centerlines, and (3) manually editing imperfect boundary lines and centerlines by hand drawings.

Since the c-DCGAN model requires 2D images as the inputs, road boundary lines and centerlines in 3D point clouds are converted into 2D images with a pixel size $S_{\epsilon 2}$. The incomplete road boundaries are broken lines, different from the road boundaries with irregular completion structures. Thus, the different training data are manually grouped into two categories, and then separately fed into the different c-DCGAN models for refinement (see Fig. 7). To obtain satisfactory completion results, the refinement results are fed into the model again to solve irregular completion structures. Finally, the road boundary refinement results are transformed back to 3D point clouds with complete structures.

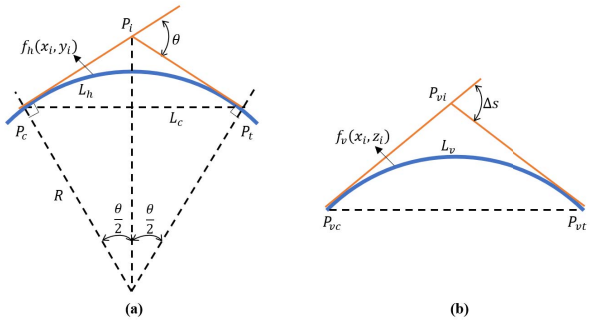

Fig. 8. (a) Elements of horizontal road geometry. (b) Elements of vertical road geometry.

D. Road Geometry Calculation

Geometric inventories of roads have remarkable impacts on road safety, and accurate road characteristics estimation, such as road width, curvature, and slope, is a vital strategy for minimizing traffic hazards and enhancing traffic efficiency. Therefore, the geometric inventory of complex urban roads (especially for curved road corridors) to estimate road characteristics contributes to road maintenance and traffic safety [10]. In this paper, based on the completed road boundaries obtained from the BoundaryNet model, some fundamental road geometries, including horizontal and vertical road alignment parameters, are thus calculated.

As illustrated in Fig. 8(a), the horizontal road geometry includes the length of horizontal curves, road width, the radius of curvature, the curvature of horizontal curves, and intersection angles. The length of a horizontal curve L_h denotes the arc length from the point of curvature P_c to the point of tangency P_t, while the radius of curvature R is the radius of the arc. The curvature of a horizontal curve C represents the average

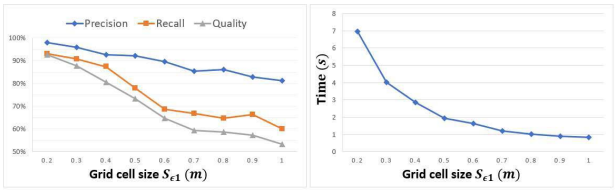

(a)

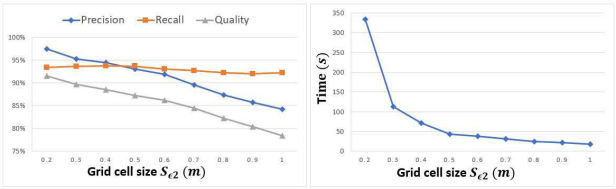

(b)

Fig. 9. Performance evaluation and time cost of the proposed models using different grid cell sizes. (a) U-shaped model for road boundary extraction. (b) c-DCGAN model for road boundary refinement.

curvature value between P_c and P_t. The intersection angle θ is the interior angle at the intersection of the two tangents.

Additionally, vertical road geometries (see Fig. 8(b)), including lengths, slope changes, and flatness, are also estimated. The length of a vertical curve L_v is calculated by using the curve integral of $f_v\ (x_i,\ z_i)$. The changes in slope Δs is the algebraic difference of the gradient between two adjacent points. The flatness of a vertical curve, also called K-value, is the flatness of the vertical arc between P_{vc} and P_{vt}. The road geometry parameters and their corresponding equations are listed in Table I.

TABLE I

DESCRIPTIONS AND EQUATIONS FOR ROAD GEOMETRY ESTIMATION

Description	Equation
Horizontal curve parameters	
Horizontal curve	$f_h\left(x_i, y_i\right) = 0$
Radius of curvature	$R = \frac{5729.58}{\theta}$
Length of horizontal curve	$L_h = 0.0174533 \times \theta \times \mathrm{R}$
Curvature of horizontal curve	$C = \left\lvert \frac{\pi - \theta}{L_h} \right\rvert$
Vertical curve parameters	
Vertical curve	$f_v\left(x_i, z_i\right) = 0$
Length of vertical curve	$L_v = \int f_v\left(x_i, z_i\right) ds$
Flatness of vertical curve	$K = \frac{L_v}{\Delta s}$

IV. RESULTS AND DISCUSSION

A. Dataset

The experimental data contains MLS point clouds and high-resolution satellite imagery. The MLS point clouds were collected from the HaiCang Industrial Park (HCIP), the Coastal Ring Road (CRR), and the International Conference and Exhibition Center (ICEC) in Xiamen, China, by using a RIEGL VMX-450 MLS system. By integrating two full-view RIEGL VQ-450 laser heads, such VMX-450 MLS system is capable of producing a maximal effective measurement rate of 1.1 million measurements/sec and a maximal scanning range up to 800 m (@150 kHz). The average point density is about 4,600 pts/m^2, and the absolute measurement accuracy and precision can reach 8 mm and 5 mm, respectively. The HCIP consists of complex road corridors and structures, the IECE has complicated urban road conditions with multiple road types, and the CRR contains multi-lane urban expressways with many roadside trees. Such road scenarios result in incomplete road boundary extraction, which makes these datasets suitable for road boundary completion evaluation. Moreover, satellite images with a ground sample distance (GSD) of 50 cm were obtained from Google Maps.

B. Hyperparameter Optimization

The developed BoundaryNet has two key hyperparameters: $S_{\epsilon 1}$, the pixel cell size in the revised U-shaped encoder-decoder for road boundary extraction; and $S_{\epsilon 2}$, the pixel cell size in the c-DCGAN model for road boundary refinement. To determine the optimal hyperparameter values, the performance of different configurations of these two parameters was evaluated on the CRR dataset during the process of road boundary line denoising and road boundary completion, respectively. The grid cell size was tested in the range of [20, 100] with an interval of 10 cm. Three evaluation metrics, including precision, recall, and quality, were utilized to quantitatively analyze road boundary extraction and refinement.

$$\text{Precision: } PR = \frac{TP}{L_{fc}} = \frac{TP}{TP + FP} \tag{7}$$

$$\text{Recall: } RE = \frac{TP}{L_{gt}} = \frac{TP}{TP + FN} \tag{8}$$

$$\text{Quality: } QU = \frac{TP}{L_{fc} + FN} = \frac{TP}{TP + FP + FN} \tag{9}$$

where TP is the length of correctly extracted boundary lines, FP is the length of the extracted boundaries that do not exist in the data, and FN is the length of the ground truth boundaries that are not extracted. L_{gt} indicates the whole length of the ground truth boundary lines, and L_{fc} represents the whole length of completed boundary lines.

Fig. 9 indicates that different grid cell sizes could deliver different performance during the phase of road boundary extraction and refinement. As shown in Fig. 9(a), all the evaluation metrics, i.e., precision, recall, and quality, achieve better results than others when setting $S_{\epsilon 1}$ at 20 cm. Although it is the most time-consuming, the time cost is still low and reasonable. Therefore, in this paper, we define $S_{\epsilon 1}$ to be 20 cm. Fig. 9(b) shows the recall of the completed road boundaries increases in the range of [20], [40], and then reduces with an increase in grid cell size $S_{\epsilon 2}$. Typically, larger grid cell sizes lead to smaller road boundary gaps. The proposed c-DCGAN model delivers better completion performance on the missing parts of smaller sizes. Still, if the grid cell size is too large, the generated road boundary images are in low-quality and coarse resolutions, resulting in incorrect gap detection and completion results.

With an increase in grid cell size, precision gradually decreases. Because larger grid cell sizes indicate that all lines in an image are thicker and coarser, it leads to the lack of boundary details. Regarding some missing parts in curved

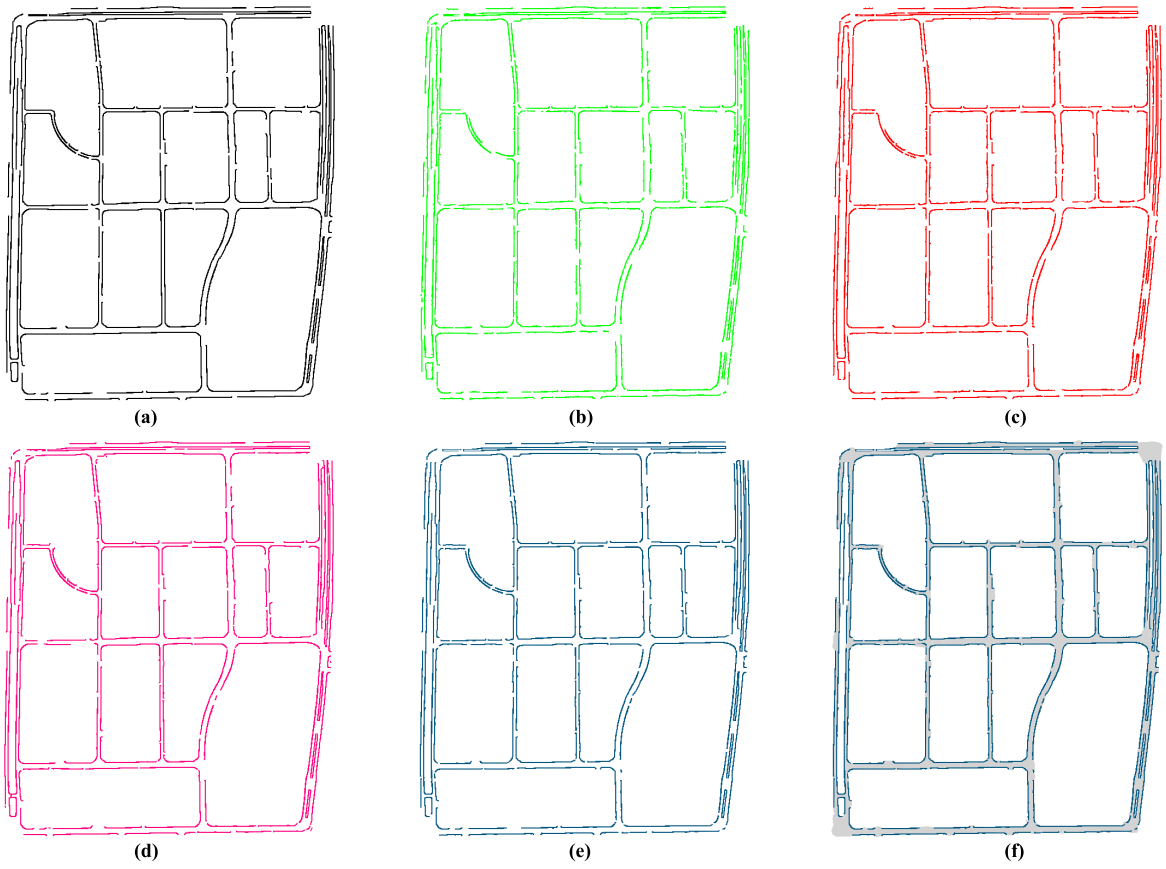

Fig. 10. The road boundary extraction results in the ICEC dataset. (a) Ground truth data (in black). (b) Road boundary extraction results obtained using Ye *et al.* [31] (in green), (c) Ma *et al.* [53] (in red), (d) Zai *et al.* [11] (in pink), and (e) Ma *et al.* [12] (in navy), respectively. (f) Road boundary completion results in the ICEC dataset based on the extracted road boundaries from Ma *et al.* (2019).

roads with small curvature, it is straightforward to restore them with straight lines directly. Fig. 9(b) illustrates that completion performance is almost the same when setting the grid cell size $S_{\epsilon 2}$ at 20 cm and 30 cm. Nevertheless, if $S_{\epsilon 2}$ is set to be 20 cm, the time cost for the c-DCGAN model is much higher than that of setting 30 cm. Hence, to achieve a balance between road boundary completion and computation efficiency, $S_{\epsilon 2}$ is set at 30 cm. Herein, to obtain a high-performance model, the segmented road boundary point clouds are first converted to the 2D images with a grid cell size of 20 cm, in which a U-shaped boundary denoising model is then conducted. Next, the correct road boundary lines are transformed back to 3D point clouds and re-projected onto the 2D images with a 30 cm grid cell size for the c-DCGAN based refinement.

C. Extraction Results

To quantitatively evaluate the proposed BoundaryNet model, the road boundary points were first manually extracted on the testing datasets. Considering the missing parts of road boundaries, points were manually added based on the road design standards and actual road conditions. To demonstrate the efficiency and robustness of the BoundaryNet model for road boundary extraction and completion in complex road environments, road boundaries with varying completeness and curvatures were extracted by using several approaches, i.e., thresholding-related [31], deep learning-related [53], supervoxel-related [11], and curb-related [12]. Fig. 10 shows the road boundary extraction results from the ICEC dataset. Accordingly, the recalls of these methods are 83.36%, 86.52%, 90.88%, and 91.12%, respectively. The higher recall of the curb-based method [12] indicates that it can robustly extract road boundaries under various curvatures with the assistance of trajectory data in urban road scenes.

D. Completion Results

Moreover, by adopting the same evaluation metrics, i.e., precision, recall, and quality, the road boundary completion results were evaluated. Figs. 11 and 12 present the boundary line completion results in the HCIP and CRR, respectively. Several common road scenarios, including straight roads, curved roads, and road intersections, were accordingly presented in zoom-in views. Although the completeness and curvatures vary in these road scenarios, the experimental results indicate that the BoundaryNet obtains good road boundary completion performance. According to three parts of initial road boundaries with varying completeness and curvatures obtained from four different methods, Table II presents the quantitative assessment on the completion results.

Regarding the BoundaryNet tested on both the HCIP and CRR datasets, depending on road boundaries extracted by

TABLE II
QUANTITATIVE ASSESSMENT ON BOUNDARY LINE COMPLETION RESULTS IN HCIP AND CRR DATASETS

Dataset	Procedure	Evaluation metric	Boundary completion process (%)			
			DL-related [53]	Thresholding-related [31]	Supervoxel-related [11]	Curb-related [12]
HCIP	Extraction results	PR	86.13	81.77	78.65	80.05
		RE	74.66	72.88	86.65	86.85
		QU	68.93	62.70	70.15	71.40
	Extraction + boundary denoising results	PR	94.55	93.41	94.45	94.81
		RE	80.16	79.26	82.81	83.31
		QU	77.23	73.82	78.97	79.69
	Extraction + boundary denoising + completion results	PR	91.09	88.82	89.87	89.89
		RE	90.17	90.66	91.34	91.40
		QU	81.52	80.74	82.81	82.88
CRR	Extraction results	PR	95.38	95.13	94.56	96.36
		RE	84.02	82.01	90.55	90.60
		QU	83.77	78.33	86.07	87.60
	Extraction + boundary denoising results	PR	97.79	98.34	97.80	97.72
		RE	84.41	80.84	85.60	85.59
		QU	82.58	80.55	83.98	83.91
	Extraction + boundary denoising + completion results	PR	94.88	93.81	95.81	96.06
		RE	91.63	89.85	92.13	92.23
		QU	85.85	82.75	88.56	88.86

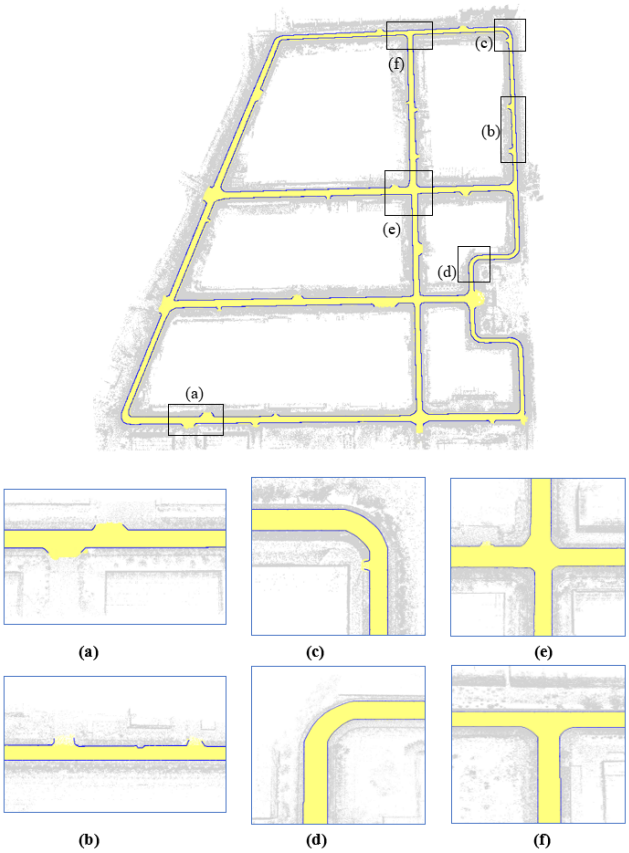

Fig. 11. Road boundary completion results using the BoundaryNet model in the HCIP dataset. (a)-(b) Straight line road sections. (c)-(d) Curved road sections. (e)-(f) Road intersections.

using the approach of Ma *et al.* [12], the precision, recall, and quality obtained on HCIP and CRR datasets are as follows: 89.89% and 96.06% in precision, respectively; 91.40% and 92.23% in recall, respectively; and 82.88% and 88.86%

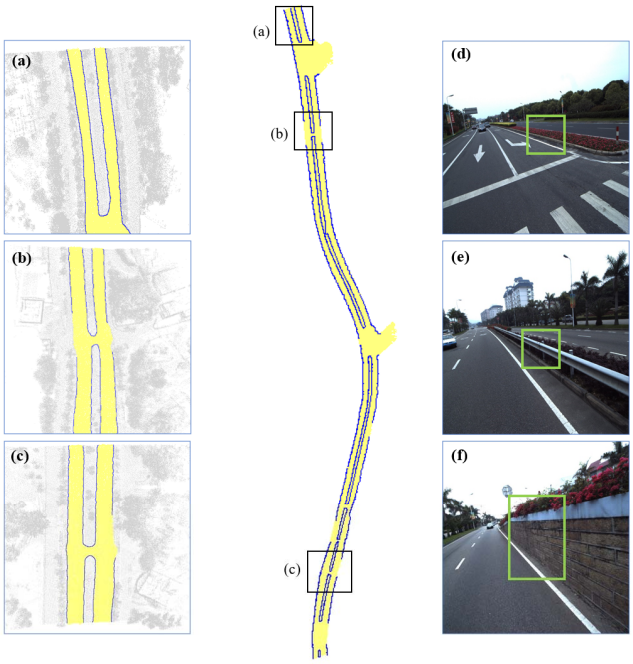

Fig. 12. Road boundary completion results using the BoundaryNet model in the CRR dataset. (a)-(c) Completion results in different road scenes. (d)-(f) Different road boundary patterns are shown in green boxes, which indicate road curbs, fences, and parapets, respectively.

in quality, respectively. Based on the experimental results, it demonstrates that the road boundary denoising process is remarkably conducive to the completion results. Additionally, the quality of initial road boundary extraction results has a significant impact on the completion performance. The lower recall of the extracted boundary lines shows a more considerable information loss in the structure of these boundaries, which causes increasing uncertainties and difficulties for road boundary completion. That is, if the initial road boundary

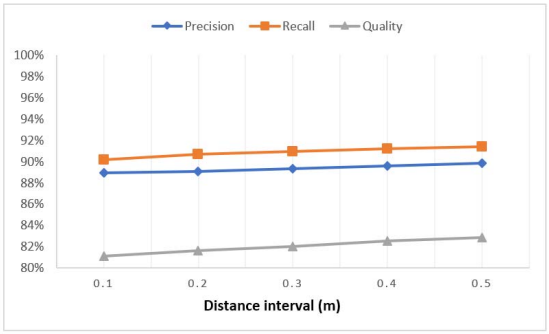

(a)

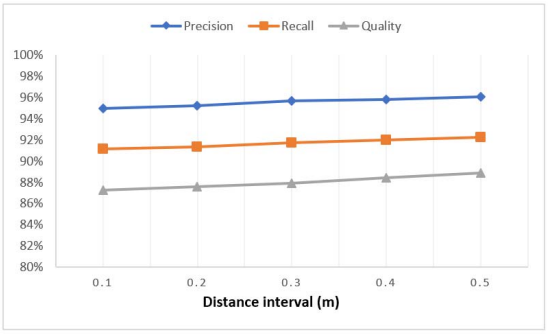

(b)

Fig. 13. Quantitative evaluation results of varying distance intervals in (a) HCIP dataset and (b) CRR dataset.

recall is low, the length of the final boundaries that exclude the ground truth boundaries (i.e., false positive) and the length of the ground truth boundaries that excludes the final completed boundaries (i.e., false negative) are large. Still, despite worn and incomplete road boundaries with a completeness rate of 59%, the BoundaryNet delivers increasing true positive results and significantly enhances recall. Therefore, the BoundaryNet achieves superior performance in road boundary completion, which can deal with incomplete road boundaries with varying completeness rates. However, some roads have occlusions and various patterns, i.e., road curbs, fences, and parapets (see Figs. 12(d)-(f)), which make the revised curb-based boundary extraction approach challenging to extract boundary lines accurately. To address this problem, multiple scans can be conducted at varying scan directions to collect more point clouds of roads, which remarkably improve the BoundaryNet model.

A comparative study was further performed focusing on the road boundary completion performance using the proposed BoundaryNet and a deep learning-based method, i.e., Wen *et al.* [8]. Both HCIP and CRR datasets were utilized to evaluate model performance. Consequently, Wen's method [8] delivered an average precision, recall, and quality of 91.03%, 89.82%, and 83.56%, respectively; while the proposed BoundaryNet model had an average precision, recall, and quality of 92.98%, 91.82%, and 85.87%, respectively. Wen's method [8] cannot effectively complement road boundaries, especially for complicated road conditions with various types of road curbs (e.g., fences, low curbs, and parapets), resulting in relatively low model performance. In contrast, the developed BoundaryNet model in this paper utilized the revised U-shaped encoder-decoder network and the c-DCGAN model to learn more inherent features and construct hierarchical feature maps among intermediate outputs, which can effectively recover the missing parts with various sizes and structures. Therefore, it leads to superior performance than Wen's method [8] for road boundary completion.

Furthermore, we also evaluated the influence of using different distance intervals in the HCIP and CRR datasets during road boundary extraction. The distance interval is determined depending on the average distance between manually edited points and their neighboring points from ground truth boundary lines. According to prior knowledge and experimental results, the distance interval defined in the results presented in Table II is 50 cm. As illustrated in Fig. 13, the increasing distance interval values contribute to the substantial improvement in precision, recall, and quality for the HCIP and CRR datasets, which indicates that manually edited points correspond well with the ground truth boundaries.

E. Road Boundary Refinement Results

In this paper, road centerlines extracted from high-resolution satellite imagery were used to enhance the completeness of road boundaries. Fig. 14 shows the results of road centerline extraction. Due to the missing parts (e.g., large gaps and irregular road structures) in the extracted road boundaries, 1,000 training samples were manually generated depending on road centerlines and boundaries, where each category has 250 positive samples and 250 negative samples. The negative samples were merged with extracted road centerlines as new training inputs to feed into the c-DCGAN boundary refinement model. Specifically, the batch size and epochs were 4 and 300, respectively.

In the testing phase, 400 negative samples were employed to examine the c-DCGAN boundary refinement performance. The generated road boundaries were evaluated by adopting the buffer-overlay-statistics (BOS) approach [54]. By specifying different buffer sizes around the manually annotated road boundaries (i.e., ground truth boundaries), the generated road boundaries after refinement were compared with ground truth boundaries through overlaying and statistics. Accordingly, the accuracy of completed road boundaries was evaluated by the miscoding, indicating what percentage of the completed road boundaries are located outside of the reference buffers. The miscoding is determined as follows:

$$\text{Miscoding} = \frac{\text{Length (L outside } C_i R \text{ in } LC_i R)}{\text{Length } (L)} \tag{10}$$

where L is the completed road boundaries, $C_i R$ is the generated buffer zones, and $LC_i R$ is a mixed dataset by overlaying L and $C_i R$.

Table III presents the quantitative assessment in miscoding for different gap categories in a part of the CRR dataset. Consequently, the miscoding in large gaps and irregular road structures is 3.98% and 4.55%, respectively, when setting the buffer size as 3 cm. The miscoding significantly decreases with increased sizes of reference buffers. Notably, for large gaps, the miscoding reduces to 0% by changing the buffer

Fig. 14. Road centerline extraction from Google Map imagery. (a) High-resolution Google Map image captured in Xiamen, China. (b) Road extraction results using the D-LinkNet model. (c) Road centerline extraction results using the morphological thinning algorithm.

TABLE III
QUANTITATIVE ASSESSMENT OF ROAD BOUNDARIES AFTER REFINEMENT IN A PART OF THE CRR DATASET

Buffer size	Miscoding	
	Large gaps	Irregular road structures
3 cm	3.98 %	4.55%
5 cm	0	2.35%
7 cm	0	0

size to 5 cm, which indicates that all road boundaries after refinement are located inside 5 cm reference buffers. Additionally, the refinement model delivers a 0% miscoding for irregular road structures by setting the buffer size 7 cm. The results demonstrate that the refinement model achieves high performance for straight road boundaries. However, it is challenging to manually annotate ground truth boundary lines in curved road sections, and a slight difference between the manually labeled boundary lines and real ground truths can lead to a large miscoding. Thus, the overall performance of the c-DCGAN refinement model is underestimated.

F. Evaluation on Paris-Lille-3D Dataset

To further demonstrate the robustness and efficiency of the BoundaryNet in relatively low-quality point clouds, we evaluated the BoundaryNet performance using the Paris-Lille-3D dataset [55]. Paris-Lille-3D point clouds were acquired in the two metropolitan cities in France, i.e., Paris and Lille, using a vehicle-borne MLS system comprising a Velodyne HDL-32E LiDAR sensor. Compared to the RIEGL VQ-450 laser scanners equipped in VMX-450 MLS systems, the Velodyne HDL-32E laser scanner is capable of delivering a maximal effective measurement rate of 0.7 million measurements per second in a scanning range up to 120 m. The average point density is about 1,500 pts/m^2, and the measurement accuracy is 2-5 cm. This Paris-Lille-3D dataset contains typical urban roadway scenarios with occlusions and various point densities and intensities, resulting in significant challenges for accurate road boundary completion. Moreover, the trajectory data was generated using the tightly-coupled GPS-RTK/INS extended Kalman filter (EKF) method assembled in the Inertial Explorer software. Thus, the road boundaries were extracted using the curb-based method [12] with fine-tuning parameters.

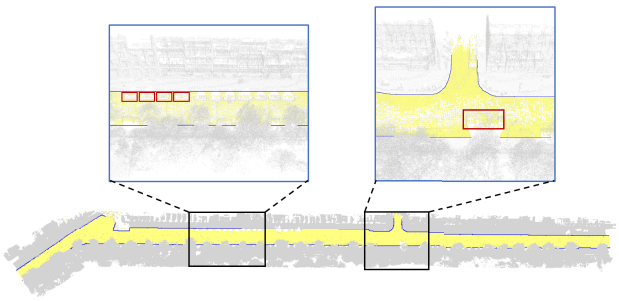

Fig. 15. Boundary line completion results using the BoundaryNet model in the Paris-Lille-3D dataset.

The boundary line completion results are shown in Fig. 15, in which two samples of typical road corridors with occlusions are enlarged for visual interpretation. Although the initial road boundaries are incomplete due to occlusions caused by street parking cars and moving trucks (see red boxes in Fig. 15), the proposed completion model can robustly and accurately recover such boundary lines. Consequently, the BoundaryNet achieves 89.31% in precision, 87.65% in recall, and 84.89% in quality in the Paris-Lille-3D dataset, respectively. Remarkably, the recall increases by 29.33% for the Paris-Lille-3D dataset after conducting road boundary denoising and completion operations, which demonstrates that the BoundaryNet can deliver a promising solution for road boundary completion in the low-quality point clouds with occlusions.

G. Road Geometry Calculation Results

In this paper, due to the lack of intuitive vertical curved road sections in four surveying areas (i.e., ICEC, HCIP, and CRR), only horizontal road alignments were estimated and evaluated. In [8], the horizontal road alignments were measured by a Leica TS-15 total station and a Leica Viva GS-15 base and rover system to achieve millimeter-level absolute measurement accuracy. Therefore, using the same testing MLS point clouds

TABLE IV
HORIZONTAL ROAD GEOMETRY CALCULATION RESULTS USING FOUR SAMPLE ROAD SECTIONS

Road sections	θ (°,′,″)			L_h (m)			C		
	Calculation	GT	Error	Calculation	GT	Error	Calculation	GT	Error
1	$120°59'56''$	$121°35'14''$	$-35'18''$	166.27	166.15	0.12	0.0062	0.0061	0.0001
2	$115°18'26''$	$114°29'22''$	$49'04''$	213.90	214.01	-0.11	0.0053	0.0053	0
3	$104°25'04''$	$104°14'54''$	$10'10''$	26.80	26.69	0.11	0.0492	0.0495	0.0003
4	$95°30'42''$	$96°00'36''$	$-29'54''$	28.69	28.77	-0.08	0.0514	0.0510	0.0004
Max Error			$49'04''$			0.12			0.0004

TABLE V
THE COMPUTATIONAL COST OF DIFFERENT PHASES FOR ROAD BOUNDARY COMPLETION IN THREE DATASETS

Dataset	Boundary completion process (s)			Time cost(s)
	U-Net denoising	CNN completion	c-DCGAN refinement	
HCIP	21.52	30.85	133.29	185.66
CRR	4.34	4.97	90.33	99.64
Paris-Lille-3D	2.83	3.45	67.46	73.74

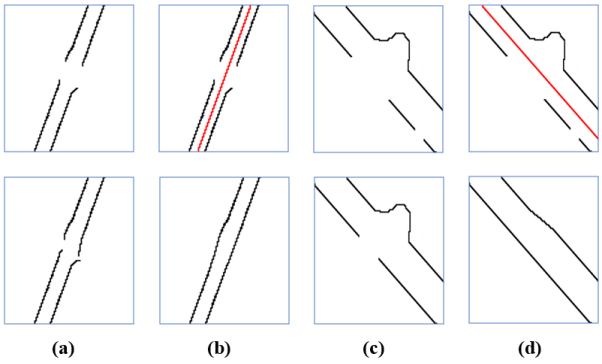

Fig. 16. Experimental results on road boundary refinement. (a-b) Training inputs of large gaps, and their boundary refinement results with and without the assistance of the road centerline (in red color), respectively. (c-d) Training inputs of irregular structures, and their boundary refinement results with and without the assistance of the road centerline (in red color), respectively.

used in [8], such manual field measurements are used as ground truth data to evaluate the performance of the proposed approach quantitatively. Table IV shows the horizontal road geometries calculated from four roads. Consequently, we delivered a maximum error of $49'04''$ for the intersection angle θ, 0.12 m for the length of horizontal curve L_h, and 0.0004 for the curvature of horizontal curve C, respectively.

H. Efficiency Evaluation

The road boundary extraction module in our developed BoundaryNet framework, programmed with C++, was debugged on a Dell desktop with an Intel® i5-7500 CPU (@3.40 GHz) and a 16 GB RAM. All CNN-based road boundary denoising, c-DCGAN based boundary completion, and D-LinkNet based road centerline extraction modules were tested using a workstation equipped with a Nvidia® Geforce 1080Ti graphic card with 12 GB memory and a 32 GB RAM. Detailed discussions about initial road boundary extraction were provided in [12]. Herein, we mainly concentrate on computational loads in the road boundary completion process. Table V indicates that the c-DCGAN road boundary refinement module, running on the GPU, consumes most of the total computational cost. In this paper, only the size of input images is considered as the primary factor that determines the time cost. The sizes of the projected road boundary lines onto 2D images in three road scenes, i.e., HCIP, CRR, and Paris-Lille-3D, are 3980 × 3660, 1876 × 5980, and 2540 × 1678, respectively. Accordingly, the HCIP dataset has the highest computational cost. Benefiting from the acceleration of the GPU, this c-DCGAN model has been boosted in a 40× faster fashion. Consequently, the total processing time for HCIP, CRR, and Paris-Lille-3D datasets are 185.66 s, 99.64 s, and 73.74 s, respectively. The proposed BoundaryNet is an offline method to fill the missing parts in the extracted road boundary lines. These total computational costs consumed in complicated urban road scenes can still meet the requirements of extensive applications, such as HD base maps.

To estimate the influence of high-resolution satellite imagery, we further evaluated the BoundaryNet completion performance with or without the assistance of road centerlines. More specifically, 150 epochs were run on the HCIP dataset. The precision, recall, and quality were accordingly recorded in Table VI. By introducing road centerlines into the BoundaryNet framework for road boundary refinement, the precision, recall, and quality increase by 1.59%, 2.48%, and 2.74%, respectively. Fig. 16 illustrates some testing results of road boundary refinement with or without using road centerlines. As can be perceived, it is very challenging to complete the missing parts, especially for irregular road structures, without

TABLE VI
PERFORMANCE EVALUATION OF THE BOUNDARYNET FRAMEWORK ON THE HCIP DATASET

Model	Evaluation metric		
	Precision(%)	**Recall** (%)	**Quality** (%)
Extraction + boundary denoising + c-DCGAN completion (without centerlines)	88.30	88.92	80.14
Extraction + boundary denoising + c-DCGAN completion (with centerlines)	89.89	91.40	82.88

the guidance of road centerlines. With the assistance of road centerlines, the c-DCGAN boundary refinement model can refine the curved roads with gaps based on the geometric characteristics of road centerlines (e.g., connectivity and curvature). The experimental results demonstrate such road centerlines extracted from high-resolution satellite imagery can significantly improve the completeness of extracted road boundaries in urban roadways.

V. CONCLUSION

This paper proposes a deep learning framework to deal with road boundary extraction and completion in complex urban road environments. These problems lead to completeness reduction and curvature loss when processing massive MLS point clouds with many missing parts, most remarkably because of the occlusions caused by road users, background interference, and incomplete data collection. We have developed a novel deep learning-based framework, named BoundaryNet, to restore 3D road boundaries by employing MLS point clouds and high-resolution satellite imagery. This BoundaryNet model provides a promising solution for 3D road boundary completion by performing a U-shaped neural network for the boundary denoising, a CNN-based network for the boundary completion, and a c-DCGAN based network with the assistance of road centerlines extracted from satellite images for the boundary refinement. Based on the completed road boundaries, the inherent road geometries are calculated.

The proposed methods have been evaluated by determining robustness and efficiency in varying road conditions (e.g., incomplete data collection and worn road curbs), which has demonstrated the superior performance of the BoundaryNet model in road boundary completion. For three highly dense MLS point clouds (i.e., HCIP, ICEC, and CRR) and a relatively low-density dataset (i.e., Paris-Lille-3D), the precision, recall, and quality obtained from HCIP, ICEC, CRR, and Paris-Lille-3D are as follows: precision: 89.89%, 89.64%, 96.06%, and 89.31%, respectively; recall: 91.40%, 91.12%, 92.23%, and 87.65%, respectively; and quality: 82.88%, 82.43%, 88.86%, and 84.89%, respectively.

Overall, it can be concluded that the developed BoundaryNet model can restore the missing parts of road boundaries under challenging road scenes more robustly, accurately, and efficiently. For further work, we will concentrate on boosting the BoundaryNet model performance by developing an end-to-end deep learning framework for 3D road boundary restoration and employing more multi-source data (e.g., open street maps, camera images, and crowd-sourced GPS data) to solve the occlusions caused by roadside objects.

REFERENCES

[1] P. Wang, T. Hunter, A. M. Bayen, K. Schechtner, and M. C. González, "Understanding road usage patterns in urban areas," *Sci. Rep.*, vol. 2, no. 1, p. 1001, Dec. 2012.
[2] S. Pu, M. Rutzinger, G. Vosselman, and S. Oude Elberink, "Recognizing basic structures from mobile laser scanning data for road inventory studies," *ISPRS J. Photogramm. Remote Sens.*, vol. 66, no. 6, pp. S28–S39, Dec. 2011.
[3] L. Ma, Y. Li, J. Li, C. Wang, R. Wang, and M. Chapman, "Mobile laser scanned point-clouds for road object detection and extraction: A review," *Remote Sens.*, vol. 10, no. 10, p. 1531, Sep. 2018.
[4] C. Ye, J. Li, H. Jiang, H. Zhao, L. Ma, and M. Chapman, "Semi-automated generation of road transition lines using mobile laser scanning data," *IEEE Trans. Intell. Transp. Syst.*, vol. 21, no. 5, pp. 1877–1890, May 2020.
[5] H. Rastiveis, A. Shams, W. A. Sarasua, and J. Li, "Automated extraction of lane markings from mobile LiDAR point clouds based on fuzzy inference," *ISPRS J. Photogramm. Remote Sens.*, vol. 160, pp. 149–166, Feb. 2020.
[6] Y. Li, L. Ma, Z. Zhong, D. Cao, and J. Li, "TGNet: Geometric graph CNN on 3-D point cloud segmentation," *IEEE Trans. Geosci. Remote Sens.*, vol. 58, no. 5, pp. 3588–3600, May 2020, doi: 10.1109/TGRS.2019.2958517.
[7] B. Pradhan and M. I. Sameen, "Road geometric modeling using laser scanning data: A critical review," in *Laser Scanning Systems in Highway and Safety Assessment*. Cham, Switzerland: Springer, 2020, pp. 15–31.
[8] C. Wen, C. You, H. Wu, C. Wang, X. Fan, and J. Li, "Recovery of urban 3D road boundary via multi-source data," *ISPRS J. Photogramm. Remote Sens.*, vol. 156, pp. 184–201, Oct. 2019.
[9] M. Soilán, A. Sánchez-Rodríguez, P. del Río-Barral, C. Perez-Collazo, P. Arias, and B. Riveiro, "Review of laser scanning technologies and their applications for road and railway infrastructure monitoring," *Infrastructures*, vol. 4, no. 4, p. 58, Sep. 2019.
[10] A. Holgado-Barco, B. Riveiro, D. González-Aguilera, and P. Arias, "Automatic inventory of road cross-sections from mobile laser scanning system," *Comput.-Aided Civil Infrastruct. Eng.*, vol. 32, no. 1, pp. 3–17, Jan. 2017.
[11] D. Zai *et al.*, "3-D road boundary extraction from mobile laser scanning data via supervoxels and graph cuts," *IEEE Trans. Intell. Transp. Syst.*, vol. 19, no. 3, pp. 802–813, Mar. 2018.
[12] L. Ma, Y. Li, J. Li, Z. Zhong, and M. A. Chapman, "Generation of horizontally curved driving lines in HD maps using mobile laser scanning point clouds," *IEEE J. Sel. Topics Appl. Earth Observ. Remote Sens.*, vol. 12, no. 5, pp. 1572–1586, May 2019.
[13] Y. Zhang, Z. Xiong, Y. Zang, C. Wang, J. Li, and X. Li, "Topology-aware road network extraction via multi-supervised generative adversarial networks," *Remote Sens.*, vol. 11, no. 9, p. 1017, Apr. 2019.
[14] W. Y. Yan, A. Shaker, and N. El-Ashmawy, "Urban land cover classification using airborne LiDAR data: A review," *Remote Sens. Environ.*, vol. 158, pp. 295–310, Mar. 2015.
[15] P. Kumar, C. P. McElhinney, P. Lewis, and T. McCarthy, "An automated algorithm for extracting road edges from terrestrial mobile LiDAR data," *ISPRS J. Photogramm. Remote Sens.*, vol. 85, pp. 44–55, Nov. 2013.
[16] X. Hu, Y. Li, J. Shan, J. Zhang, and Y. Zhang, "Road centerline extraction in complex urban scenes from LiDAR data based on multiple features," *IEEE Trans. Geosci. Remote Sens.*, vol. 52, no. 11, pp. 7448–7456, Nov. 2014.
[17] M. Hashemi, "Automatic inference of road and pedestrian networks from spatial-temporal trajectories," *IEEE Trans. Intell. Transp. Syst.*, vol. 20, no. 12, pp. 4604–4620, Dec. 2019.
[18] R. Qin and A. Gruen, "3D change detection at street level using mobile laser scanning point clouds and terrestrial images," *ISPRS J. Photogramm. Remote Sens.*, vol. 90, pp. 23–35, Apr. 2014.
[19] Y. Li, L. Xiang, C. Zhang, and H. Wu, "Fusing taxi trajectories and RS images to build road map via DCNN," *IEEE Access*, vol. 7, pp. 161487–161498, 2019.

[20] R. Ravi *et al.*, "Lane width estimation in work zones using LiDAR-based mobile mapping systems," *IEEE Trans. Intell. Transp. Syst.*, vol. 21, no. 12, pp. 5189–5212, Dec. 2020, doi: 10.1109/TITS.2019.2949762.

[21] Z. Chen, W. Fan, B. Zhong, J. Li, J. Du, and C. Wang, "Corse-to-fine road extraction based on local Dirichlet mixture models and multiscale-high-order deep learning," *IEEE Trans. Intell. Transp. Syst.*, vol. 21, no. 10, pp. 4283–4293, Oct. 2020.

[22] J. Wang, J. Song, M. Chen, and Z. Yang, "Road network extraction: A neural-dynamic framework based on deep learning and a finite state machine," *Int. J. Remote Sens.*, vol. 36, no. 12, pp. 3144–3169, Jun. 2015.

[23] Y. Kang, C. Roh, S.-B. Suh, and B. Song, "A lidar-based decision-making method for road boundary detection using multiple Kalman filters," *IEEE Trans. Ind. Electron.*, vol. 59, no. 11, pp. 4360–4368, Nov. 2012.

[24] B. Yang, L. Fang, and J. Li, "Semi-automated extraction and delineation of 3D roads of street scene from mobile laser scanning point clouds," *ISPRS J. Photogramm. Remote Sens.*, vol. 79, pp. 80–93, May 2013.

[25] C. Cabo, A. Kukko, S. García-Cortés, H. Kaartinen, J. Hyyppä, and C. Ordoñez, "An algorithm for automatic road asphalt edge delineation from mobile laser scanner data using the line clouds concept," *Remote Sens.*, vol. 8, no. 9, p. 740, Sep. 2016.

[26] Y. Lin, W. Cheng, D. Zhai, L. Wei, and J. Li, "Toward better boundary preserved supervoxel segmentation for 3D point clouds," *ISPRS J. Photogramm. Remote Sens.*, vol. 143, pp. 39–47, Sep. 2018.

[27] N. Homayounfar, W.-C. Ma, S. K. Lakshmikanth, and R. Urtasun, "Hierarchical recurrent attention networks for structured online maps," in *Proc. IEEE/CVF Conf. Comput. Vis. Pattern Recognit.*, Jun. 2018, pp. 3417–3426.

[28] J. Liang, N. Homayounfar, W.-C. Ma, S. Wang, and R. Urtasun, "Convolutional recurrent network for road boundary extraction," in *Proc. IEEE/CVF Conf. Comput. Vis. Pattern Recognit. (CVPR)*, Jun. 2019, pp. 9512–9521.

[29] Y. Zang, C. Wang, Y. Yu, L. Luo, K. Yang, and J. Li, "Joint enhancing filtering for road network extraction," *IEEE Trans. Geosci. Remote Sens.*, vol. 55, no. 3, pp. 1511–1525, Mar. 2017.

[30] H. Chu *et al.*, "Neural turtle graphics for modeling city road layouts," in *Proc. IEEE ICCV*, 2019, pp. 4522–4530.

[31] C. Ye *et al.*, "Robust lane extraction from MLS point clouds towards HD maps especially in curve road," *IEEE Trans. Intell. Transp. Syst.*, early access, Nov. 10, 2020, doi: 10.1109/TITS.2020.3028033.

[32] A. Boyko and T. Funkhouser, "Extracting roads from dense point clouds in large scale urban environment," *ISPRS J. Photogramm. Remote Sens.*, vol. 66, no. 6, pp. S2–S12, Dec. 2011.

[33] S. Gu, Y. Zhang, J. Yang, J. M. Alvarez, and H. Kong, "Two-view fusion based convolutional neural network for urban road detection," in *Proc. IEEE IROS*, Nov. 2019, pp. 6144–6149.

[34] S. Gu, Y. Zhang, J. Tang, J. Yang, and H. Kong, "Road detection through CRF based Lidar-camera fusion," in *Proc. ICRA*, 2019, pp. 3832–3838.

[35] D. Yu, H. Xiong, Q. Xu, J. Wang, and K. Li, "Multi-stage residual fusion network for LIDAR-camera road detection," in *Proc. IEEE Intell. Vehicles Symp. (IV)*, Jun. 2019, pp. 2323–2328.

[36] B. Li *et al.*, "Virtual lane boundary generation for human-compatible autonomous driving: A tight coupling between perception and planning," in *Proc. IEEE/RSJ Int. Conf. Intell. Robots Syst. (IROS)*, Nov. 2019, pp. 3733–3739.

[37] S. Xu, R. Wang, and H. Zheng, "Road curb extraction from mobile LiDAR point clouds," *IEEE Trans. Geosci. Remote Sens.*, vol. 55, no. 2, pp. 996–1009, Feb. 2017.

[38] P. Kumar, C. P. McElhinney, P. Lewis, and T. McCarthy, "Automated road markings extraction from mobile laser scanning data," *Int. J. Appl. Earth Observ. Geoinf.*, vol. 32, pp. 125–137, Oct. 2014.

[39] M. Soilán, B. Riveiro, J. Martínez-Sánchez, and P. Arias, "Segmentation and classification of road markings using MLS data," *ISPRS J. Photogramm. Remote Sens.*, vol. 123, pp. 94–103, Jan. 2017.

[40] J. Jung, E. Che, M. J. Olsen, and C. Parrish, "Efficient and robust lane marking extraction from mobile lidar point clouds," *ISPRS J. Photogramm. Remote Sens.*, vol. 147, pp. 1–18, Jan. 2019.

[41] O. Ronneberger, P. Fischer, and T. Brox, "U-net: Convolutional networks for biomedical image segmentation," in *Proc. MICCAI*. Cham, Switzerland: Springer, 2015, pp. 234–241.

[42] F. Milletari, N. Navab, and S.-A. Ahmadi, "V-net: Fully convolutional neural networks for, volumetric medical image segmentation," in *Proc. 4th Int. Conf. 3D Vis. (3DV)*, 2016, pp. 565–571.

[43] P. Isola, J.-Y. Zhu, T. Zhou, and A. A. Efros, "Image-to-image translation with conditional adversarial networks," in *Proc. IEEE ICCV*, 2017, pp. 1125–1134.

[44] J. Yu, Z. Lin, J. Yang, X. Shen, X. Lu, and T. S. Huang, "Free-form image inpainting with gated convolution," in *Proc. IEEE CVPR*, 2019, pp. 4471–4480.

[45] K. Nazeri, E. Ng, T. Joseph, F. Qureshi, and M. Ebrahimi, "Edgeconnect: Structure guided image inpainting using edge prediction," in *Proc. IEEE CVPR*, 2019, pp. 3265–3274.

[46] K. Sasaki, S. Iizuka, E. Simo-Serra, and H. Ishikawa, "Learning to restore deteriorated line drawing," *Vis. Comput.*, vol. 34, nos. 6–8, pp. 1077–1085, 2018.

[47] D. Pathak, P. Krahenbuhl, J. Donahue, T. Darrell, and A. A. Efros, "Context encoders: Feature learning by inpainting," in *Proc. IEEE CVPR*, 2016, pp. 2536–2544.

[48] L. Zhou, C. Zhang, and M. Wu, "D-LinkNet: LinkNet with pretrained encoder and dilated convolution for high resolution satellite imagery road extraction," in *Proc. IEEE/CVF Conf. Comput. Vis. Pattern Recognit. Workshops (CVPRW)*, Jun. 2018, pp. 182–186.

[49] K. He, X. Zhang, S. Ren, and J. Sun, "Deep residual learning for image recognition," in *Proc. IEEE Conf. Comput. Vis. Pattern Recognit. (CVPR)*, Jun. 2016, pp. 770–778.

[50] I. Demir *et al.*, "DeepGlobe 2018: A challenge to parse the Earth through satellite images," in *Proc. IEEE/CVF Conf. Comput. Vis. Pattern Recognit. Workshops (CVPRW)*, Jun. 2018, pp. 172–181.

[51] W. Shi, Z. Miao, and J. Debayle, "An integrated method for urban main-road centerline extraction from optical remotely sensed imagery," *IEEE Trans. Geosci. Remote Sens.*, vol. 52, no. 6, pp. 3359–3372, Jun. 2014.

[52] I. Goodfellow, J. Pouget-Abadie, M. Mirza, B. Xu, D. Warde-Farley, S. Ozair, A. Courville, and Y. Bengio, "Generative adversarial nets," in *Proc. Adv. Neural Inf. Process. Syst.*, 2014, pp. 2672–2680.

[53] L. Ma *et al.*, "Capsule-based networks for road marking extraction and classification from mobile LiDAR point clouds," *IEEE Trans. Intell. Transp. Syst.*, early access, May 6, 2020, doi: 10.1109/TITS.2020.2990120.

[54] H. Tveite, "An accuracy assessment method for geographical line data sets based on buffering," *Int. J. Geographical Inf. Sci.*, vol. 13, no. 1, pp. 27–47, Jan. 1999.

[55] X. Roynard, J.-E. Deschaud, and F. Goulette, "Paris-Lille-3D: A large and high-quality ground-truth urban point cloud dataset for automatic segmentation and classification," *Int. J. Robot. Res.*, vol. 37, no. 6, pp. 545–557, May 2018.

Lingfei Ma (Student Member, IEEE) received the B.Sc., M.Sc., and Ph.D. degrees in geomatics engineering from the University of Waterloo, Waterloo, ON, Canada, in 2015, 2017, and 2020, respectively.

He is currently an Assistant Professor of Urban Data Science with the Central University of Finance and Economics, Beijing, China. His research interests include autonomous driving, mobile laser scanning, intelligent processing of point clouds, 3D scene modeling, and machine learning. He has published more than 20 papers in refereed journals and conferences, including IEEE TRANSACTIONS ON INTELLIGENT TRANSPORTATION SYSTEMS (TITS), IEEE TRANSACTIONS ON GEOSCIENCE AND REMOTE SENSING (TGRS), ISPRS-JPRS, IEEE TRANSACTIONS ON NEURAL NETWORKS AND LEARNING SYSTEMS (TNNLS), and IEEE-CVPRW.

Ying Li received the B.Eng. degree in geomatics engineering from the Hefei University of Technology, China, in 2014, and the M.Sc. degree in remote sensing from Wuhan University, China, in 2017. She is currently pursuing the Ph.D. degree with the Mobile Sensing and Geodata Science Laboratory, Department of Geography and Environmental Management, University of Waterloo, Waterloo, ON, Canada.

Her research interests include autonomous driving, mobile laser scanning, intelligent processing of point clouds, geometric and semantic modeling, and augmented reality.

Jonathan Li (Senior Member, IEEE) received the Ph.D. degree in geomatics engineering from the University of Cape Town, Cape Town, South Africa, in 2000.

He is currently a Professor and the Head of the Mobile Sensing and Geodata Science Group, Department of Geography and Environmental Management, cross-appointed with the Department of Systems Design Engineering, University of Waterloo, Waterloo, ON, Canada. He is also Founding Member of the Waterloo Artificial Intelligence Institute. His research interests include AI-based information extraction from mobile LiDAR point clouds and Earth observation images. He has coauthored more than 400 publications, more than 200 of which were published in refereed journals, including IEEE TRANSACTIONS ON GEOSCIENCE AND REMOTE SENSING (TGRS), IEEE TRANSACTIONS ON INTELLIGENT TRANSPORTATION SYSTEMS (TITS), IEEE JOURNAL OF SELECTED TOPICS IN APPLIED EARTH OBSERVATIONS AND REMOTE SENSING (JSTARS), IEEE GEOSCIENCE AND REMOTE SENSING LETTERS (GRSL), ISPRS-JPRS, and RSE. He is the Chair of the ISPRS WG I/2 on LiDAR, Air- and Space-borne Optical Sensing, from 2016 to 2020, and has been the ICA Commission on Sensor-driven Mapping since 2015. He is an Associate Editor of the IEEE TRANSACTIONS ON INTELLIGENT TRANSPORTATION SYSTEMS (TITS), IEEE JOURNAL OF SELECTED TOPICS IN APPLIED EARTH OBSERVATIONS AND REMOTE SENSING (JSTARS), and *Canadian Journal of Remote Sensing*. He was a recipient of the Outstanding Achievement in Mobile Mapping Technology Award in 2019 for his pioneering contributions in developing and promoting mobile mapping technology and the ISPRS Samuel Gamble Award in 2020 for his significant contributions to the development, organization or professional activities of the photogrammetry, remote sensing, and spatial information sciences at national or international level.

José Marcato Junior (Member, IEEE) received the Ph.D. degree in cartographic science from Sao Paulo State University, Brazil. He is currently a Professor with the Faculty of Engineering, Architecture and Urbanism and Geography, Federal University of Mato Grosso do Sul, Campo Grande, Brazil. His current research interests include UAV photogrammetry and deep neural networks for object detection, classification, and segmentation. He has published more than 30 in refereed journals and more than 70 in conferences, including *ISPRS Journal of Photogrammetry and Remote Sensing*, and IEEE JOURNAL OF SELECTED TOPICS IN APPLIED EARTH OBSERVATIONS AND REMOTE SENSING.

Wesley Nunes Gonçalves (Member, IEEE) received the Ph.D. degree in computational physics from the University of Sao Paulo, Brazil. He is currently a Professor with the Faculty of Computer Science and Faculty of Engineering, Architecture and Urbanism and Geography, Federal University of Mato Grosso do Sul, Campo Grande, Brazil. His current research interests include computer vision, machine learning, deep neural networks for object detection, classification, and segmentation. He has published more than 30 in refereed journals and more than 60 in conferences, including *Pattern Recognition*, *Pattern Recognition Letters*, and *Neurocomputing*.

Michael A. Chapman (Senior Member, IEEE) received the Ph.D. degree in photogrammetry from Laval University, Qubec City, QC, Canada.

He was a Professor with the Department of Geomatics Engineering, University of Calgary, Calgary, AB, Canada, for 18 years prior joining Ryerson University, Toronto, ON, Canada, in 1999. He is currently a Professor with the Department of Civil Engineering, Ryerson University. He has authored or coauthored more than 200 technical articles, including those in top remote sensing journals, such as *ISPRS Journal of Photogrammetry and Remote Sensing* and IEEE TRANSACTIONS ON GEOSCIENCE AND REMOTE SENSING. His research interests include algorithms and processing methodologies for airborne sensors using GNSS/IMU, geometric processing of digital imagery in industrial environments, terrestrial imaging systems for transportation infrastructure mapping, mobile laser scanning, and algorithms and processing strategies for biometrology applications.